

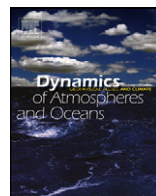


ELSEVIER

Contents lists available at ScienceDirect

## Dynamics of Atmospheres and Oceans

journal homepage: [www.elsevier.com/locate/dynatmoce](http://www.elsevier.com/locate/dynatmoce)



# Near real-time ocean circulation assimilation and prediction in the Intra-Americas Sea with ROMS

B.S. Powell<sup>a,\*</sup>, A.M. Moore<sup>b</sup>, H.G. Arango<sup>c</sup>, E. Di Lorenzo<sup>d</sup>, R.F. Milliff<sup>e</sup>,  
R.R. Leben<sup>f</sup>

<sup>a</sup> Dept. of Oceanography, University of Hawaii, Manoa, HI, United States

<sup>b</sup> Dept. of Ocean Sciences, University of California at Santa Cruz, United States

<sup>c</sup> Institute of Marine and Coastal Sciences, Rutgers University, NJ, United States

<sup>d</sup> School of Earth and Atmospheric Sciences, Georgia Institute of Technology, United States

<sup>e</sup> NWRA, Colorado Research Associates Division, Boulder, CO, United States

<sup>f</sup> Colorado Center for Astrodynamics Research, University of Colorado, Boulder, CO, United States

## ARTICLE INFO

### Article history:

Available online 3 May 2009

### Keywords:

Data assimilation

Ensemble forecasting

Ocean prediction

Intra-Americas Sea

4DVAR

ROMS

Real-time observations

## ABSTRACT

We present the feasibility of a prototype, near real-time assimilation and ensemble prediction system for the Intra-Americas Sea run autonomously aboard a ship of opportunity based on the Regional Ocean Modeling System (ROMS). Predicting an ocean state depends upon numerical models that contain uncertainties in their modeled physics, initial conditions, and model state. An advanced model, four-dimensional variational assimilation, and ensemble forecasting techniques are used to account for each of these uncertainties. Every 3 days, data from the previous 7 days period were assimilated to generate an estimate of the circulation and to create an ensemble of 2 weeks forecasts of the ocean state. This paper presents the methods and results for a multi-resolution assimilation system and ensemble forecasts of surface fields and dominant surface circulation features. When compared to post-processed science quality observations, the state estimates suffer from our reliance on real-time, quick-look satellite observations of the ocean surface. Despite a number of issues, the ensemble forecast estimate is often superior to observational persistence. This proof-of-concept prototype performed well enough to reveal deficiencies, provide useful insights, valuable lessons, and guidance for future improvements in real-time ocean forecasting.

© 2009 Elsevier B.V. All rights reserved.

\* Corresponding author.

E-mail address: [powellb@hawaii.edu](mailto:powellb@hawaii.edu) (B.S. Powell).

## 1. Introduction

Prediction of the ocean or atmosphere involves a complex, nonlinear system with imperfect physics, and uncertainties in the model state and boundary and initial conditions. Since the 1970s, significant progress against each of these issues has improved model predictive skill in numerical weather prediction (Kalnay et al., 1998; Buizza et al., 2000; Simmons and Hollingsworth, 2002). Advancements in computational power and numerical schemes have helped reduce the uncertainties in model physics. Advanced variational data assimilation techniques have done much to address the errors in the current state estimate (Le Dimet and Talagrand, 1986; Talagrand and Courtier, 1987; Courtier et al., 1994; Chua and Bennett, 2001). Ensemble techniques provide forecast estimates of probability distribution functions that are consistent with the estimates of the model state errors (Lewis, 2005). The practice of using numerical weather forecasting in the ocean is relatively new and actively under development (Pinardi and Woods, 2002; Chassignet and Verron, 2006). We present a near real-time ocean prediction system that incorporates an advanced primitive equation model, multi-resolution four-dimensional variational (4DVAR) data assimilation, and ensemble prediction methods running aboard a ship at sea. Our previous work, Powell et al. (2008) (hereafter P2008), presented the theory and application results of the incremental 4DVAR assimilation method in ROMS. This paper presents an operational forecasting system comprised of a multi-resolution assimilation scheme, a method for ensemble forecasts using information derived from the assimilation procedure, and serving to elucidate the challenges, issues and options available with respect to real-time ocean forecasts of surface fields while operating at sea.

The focus of this study is the Intra-Americas Sea (IAS), shown in Fig. 1, which encompasses the Gulf of Mexico (GOM) and Caribbean Sea and contains five deep basins separated by relatively shallow sills (<2000 m). The IAS circulation is an important component of the western boundary current system of the North Atlantic sub-tropical gyre (Lee et al., 1996) and is fed by ocean transport through the Antilles island passages. This flow converges in the northwest Caribbean as the Yucatan Current to become the Loop Current (LC), the energetic jet entering the Gulf of Mexico through the Yucatan Channel and separating from the Campeche Bank. The LC is the dominant source of energy, variability, and momentum that drives much of the circulation within the Gulf of Mexico (Ohlmann et al., 2001; Schmitz et al., 2005). The LC exits through the Florida Straits and proceeds north as the Gulf Stream. The circulation is characterized by a richly varied dynamical structure of energetic, large-scale, mesoscale and submesoscale eddies (Moore and Maul, 1998; Schmitz et al., 2005).

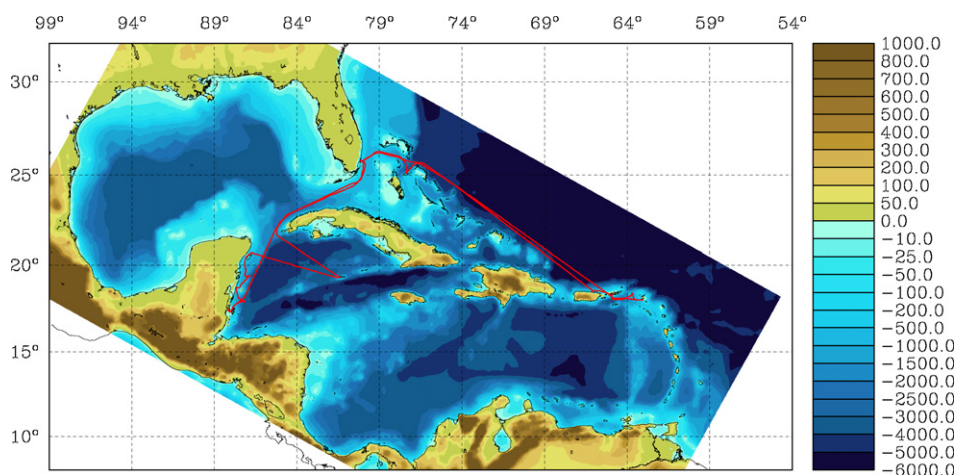


**Fig. 1.** The model domain encompasses the entirety of the IAS and portions of the North Atlantic. The western and eastern cruise tracks followed by the Royal Caribbean International *Explorer of the Seas* are indicated by the red lines.

Ocean assimilation and prediction systems have been in use for several years, and there are a number of notable systems already operating in the GOM or IAS including: The Hybrid Coordinate Ocean Model (HYCOM) Data Assimilation and Prediction System runs globally with a number of higher-resolution regional products (including the GOM) using an optimal interpolation based assimilation procedure (Chassignet et al., 2007; Metzger et al., 2008). Ko et al. (2007) runs a near real-time assimilation and prediction system in the IAS and coast of Portugal using a nudging procedure. The University of Rhode Island in collaboration with NOAA has developed an operational ocean-hurricane coupled prediction system (Bender et al., 2007) that assimilates SST data through a field replacement procedure Bender and Ginis (2000). A full review of GOM prediction systems is found in Chassignet et al. (2005). The variational assimilation procedure used in this paper differs in that it uses the dynamics of the model to constrain the assimilation procedure (see P2008).

The prototype, autonomous data assimilation and ensemble forecasting system described here was run on a single, quad-CPU computer system installed in the Ocean Lab aboard the Royal Caribbean International ship *Explorer of the Seas*, a ship of opportunity operating in the IAS. An important facet for this Office of Naval Research (ONR) funded study was to determine the efficacy of autonomous, ship-board, near real-time predictions of surface currents and dominant circulation features, and as such, the system ran on-board displaying the latest estimates available. The availability of near real-time ADCP observations and the ship-board Ocean Lab facility were a significant factor for deploying this experiment onboard rather than on land; unfortunately, soon into the experiment, the *Explorer of the Seas* was moved to a different cruise track outside of the IAS region and ADCP data were not available. In addition to developing the autonomous, stand-alone system, the equipment was available for ship-board research and outreach activities with the cruise passengers. The forecast information was presented publicly in real-time (both onboard and via the website); however, owing to its commercial nature, predictions did not influence the operation of the ship. The available computing resources onboard the ship and the near real-time requirement placed significant constraints on the approach used for this work including the resolution of the model, choices of error statistics, data handling, etc.

The prototype system was designed to autonomously ingest real-time daily satellite maps of sea surface height (SSH) and sea surface temperature (SST). Each day, the ship-board computer transferred the latest data via a satellite link from various land-based servers, and performed the necessary data processing.

During each cycle, observations from the preceding 7 days (including the current day) were assimilated into the model to compute a nowcast of the IAS circulation to serve as the initial condition for a forecast. A forecast ensemble comprised of 41 members was created by randomly sampling the ocean state probability distribution using estimates of uncertainty in the current state computed during the assimilation procedure. With the limited computing power onboard, nearly 3 days were required to complete a full assimilation and ensemble prediction cycle; therefore, two assimilation and prediction cycles were run each week.

The system was designed to be fully autonomous, and it downloaded the required observations, atmospheric forcing and forecasts, as well as updated the public website on a daily basis. Every day, the system processed all data required for the assimilation and ensemble prediction cycles. The processing cycle ran continuously and included numerous computing processes to monitor and manage the assimilation procedure, build the ensemble members, time integrate the ensemble members, and generate the real-time output displayed in the Ocean Lab for travellers on-board the *Explorer of the Seas* (some 2,000 visitors attended daily briefings over the initial 6-week period) as well as updating the monitoring website onshore.

The configuration and results from the prototype near real-time assimilation and prediction system as it ran aboard the *Explorer of the Seas* from January through July 2007 are presented. The goal during the initial phase of this experiment was to explore the theory and challenges of applying a sophisticated multi-resolution assimilation and prediction system, similar to that used in numerical weather prediction, in a real-time ocean-going environment. Numerical modeling, variational data assimilation, and ensemble prediction are active fields of research, and combining them is a complex and technically challenging task. Section 2 presents the model and data used in the experiment. Section 3 provides a description and results of the near real-time multi-resolution assimilation procedure.

The ensemble predictions made from the assimilated initial conditions are described and analyzed in Section 4. A summary and conclusions follow in 5.

## 2. Regional Ocean Modeling System (ROMS) and observational data

The Regional Ocean Modeling System (ROMS) is a free-surface, hydrostatic, primitive equation model discretized with a terrain following vertical coordinate system (Shchepetkin and McWilliams, 2005; Haidvogel et al., 2008), and it has been used to model many regions of the world ocean.<sup>1</sup> ROMS is characterized by advanced numerical techniques that are designed to minimize computational errors (Shchepetkin and McWilliams, 2003).

The same model setup as presented in P2008 is used at both  $1/3^\circ$  and  $1/6^\circ$  horizontal resolutions with 30 s levels. The models use third-order horizontal advection with the generic length scale vertical mixing scheme (Warner et al., 2005) using  $k$ – $kl$  mixing coefficients (corresponding to Mellor–Yamada Level 2.5). The ocean surface heat flux is computed via the COARE algorithm (Fairall et al., 1996). To allow for known uncertainties in the net surface freshwater flux and the lack of fresh water discharge data, the model surface salinity is relaxed to the monthly Levitus climatology (Levitus et al., 1994) with a relaxation time of 50 days.

The model boundary conditions were configured to conserve volume via a Chapman condition on the free surface, a Flather condition for the 2D momentum, and clamped to the 3D momentum and tracers. The data for the clamped boundary conditions were derived from a long North Atlantic ROMS simulation run at  $1/6^\circ$  with NCEP forcing (Haidvogel et al., 2000). Climatological boundaries were used because near real-time boundary data are not available during the forecast periods.

During each assimilation cycle, the ocean was forced using the real-time NCEP global data assimilation product (NCEP–GDAS), at  $2.5^\circ$  spatial resolution available every 12 h. During the forecast period, the model was forced by the 16 days, NCEP global forecasting system (NCEP–GFS) near real-time product, at  $2^\circ$  resolution, available every 12 h.

### 2.1. Limit of deterministic predictability

To determine the potential predictive skill of the model, it is important to quantify the time-scales over which model fields become decorrelated (Daley, 1991): the limit of deterministic predictability. The growth of uncertainties in the initial state, forcing, and boundary conditions will drive the error in the model forecast to this limit, at which time the forecast contains no useful information.

We denote  $\Psi$  as the ocean state vector comprising all prognostic fields ( $\zeta, u, v, T, S$ ) at each grid point, and  $\Psi(t)$  represents the time-dependent circulation over the interval  $t = [t_1, t_2]$ . As shown by Daley (1991), the limit of deterministic predictability can be estimated from a sample of randomly chosen states by considering the mean squared difference:

$$\sigma^2 = \frac{1}{N} \sum_{i=1}^N (\Psi_f(t_1) - \Psi_f(t_2))^2, \quad (1)$$

where  $f$  is the prognostic variable of choice (such as SST or SSH points),  $N$  are the number of  $f$  points in the vector, and  $t_1, t_2$  are chosen within the same season to avoid a seasonal bias in  $\sigma^2$ . For many random pairs,  $\sigma^2$  defines the climatological variance of the circulation. We note that Daley (1991) calculated the climatological variance using an energy norm of the entire state; however, this work uses the Euclidian (or  $L_2$ ) norm. With the  $L_2$  norm, individual fields (SSH and SST) of the state pairs are compared independently, which leads to differing limits of predictability for each field.

<sup>1</sup> see <http://www.myroms.org/papers>.

Using 5000 random combinations of state pairs from a 15-year, non-assimilating model spinup, the climatological variance for SSH (SST) is found to be 17.7 cm (1.18 °C), which is found for states separated by a minimum of approximately 45 (21) days. In the ocean, the limit of deterministic predictability is strongly influenced by the atmospheric forcing, which can push a perturbed ocean state back towards a background mean flow, and later sections will show how this influences the forecasts.

Another useful concept is that of the persistence forecast (Wilks, 1995) for which the observed state of the system at a given time,  $\Psi^{\text{obs}}(t_1)$  is used as the future state,  $\Psi(t)$  (i.e.,  $\Psi^{\text{obs}}(t_1)$  is “persisted” over the forecast interval  $t = [t_1, t_2]$ ). It is easy to show that the error variance of the persistence forecast will asymptote to the climatological variance as the interval increases. Persistence forecasts are used as a benchmark for forecast models, while the limit of deterministic predictability is the time limit beyond which one cannot reasonably expect to forecast the ocean state.

## 2.2. Observational data

The near real-time SSH anomaly data were provided by the Colorado Center for Astrodynamics (CCAR) at the University of Colorado (Leben et al., 2002). The merged data from the real-time altimeter streams are created on a daily basis, providing maps of daily observed SSH anomalies. This merged product uses the Jason-1, Envisat, and GEOSAT Follow-On (GFO) satellites. These anomalies are relative to the Goddard Space Flight Center SSH mean (Wang, 2001). The data are available as daily composites on a 0.25° grid. The product uses an iterative optimal interpolation scheme to blend the multiple observations which results in different characteristics than products using a standard Kriging based optimal interpolation (Leben et al., 2002). Although alongtrack altimetry data is preferable, due to the limited availability of real-time altimetry data at the time, we chose to use this freely available mapped product.

Starting in November 2006, the Jason-1 real-time orbital information was seriously degraded due to the diminished tracking ability of the onboard GPS receiver (S. Desai, personal communication). This fault required that the CCAR near real-time data system switch to the Interim Geophysical Data Record stream. This hardware problem does not impact delayed science products because the orbital information can be accurately resolved in post-processing; however, this has a severe impact on the estimate of SSH in near real-time, especially during time periods when additional sampling is not available from GFO or Envisat. Coincidentally, the Geosat Follow-on (GFO) satellite was offline due to power problems from January 2007 into April 2007. The data latency and the data outage combined to seriously degrade the real-time SSH data available for this experiment during the initial 3 months of the experiment, and the forecast performance echoes these problems.

As in P2008, SSH anomalies were converted into total dynamic height to be consistent with the model by removing the steric signal using the Willis et al. (2004) database, and they were added to a mean dynamic height from the model generated from the 16 years, forward model run from 1990 through 2006 subject only to NCEP surface forcing. These processed SSH fields were assimilated into the model.

Near real-time sea surface temperature (SST) measurements were provided by the GODAE High Resolution SST Pilot Program (GHRST-PP) (Donlon et al., 2007). The GHRST-PP L4 data are available daily at 1/20° updated with observations taken in the previous 24 h and combines all available satellite SST measurements (including infrared and microwave) with *in situ* measurements using a temporal and spatial optimal interpolation scheme (Donlon, 2006). Similar to the alongtrack altimetry, the limited resources available onboard prevented us from using real-time satellite swaths from the available microwave and infrared satellite instruments.

The two real-time satellite products utilize spatial and temporal optimal interpolation to generate surface maps (Leben et al., 2002; Donlon, 2006); however, due to their real-time nature, the time window is not centered and weights the real-time data higher. Furthermore, both use quicklook satellite data and do not benefit from the post-processed science quality satellite products that are produced by the respective data centers. These issues have the potential to introduce aliasing and measurement errors.

### 2.3. Verification data

Due to the errors in the near real-time quicklook products, the two separate time-delayed data sources used in P2008 are considered the GODAE merged altimeter SSH anomaly product distributed by Aviso is used for SSH verification. These data are available as daily composites at  $0.3^\circ$  and are delayed approximately one month from the current day. For SST verification, a blended microwave and infrared product from David Foley (Foley-SST) of the National Oceanic and Atmospheric Administration is used. This product is provided as a daily, 5-day composite at  $0.1^\circ$  spatial resolution and is delayed 2–3 days from the current.

Powell and Moore (2009) found the RMS difference (RMSD) between the observational products to be significant for SSH ( $\sim 10$  cm during the period of degraded near real-time performance) and SST ( $0.65^\circ\text{C}$ ) in the IAS. Because the delayed products utilize science quality data, they are used as an independent estimate of the ocean state when computing the error statistics in Sections 3.2 and 4. Although the verification data and observational data are each derived using some overlapping data from identical observational platforms, the significant RMSD between them suggest that due to the different optimal interpolation techniques, science quality versus first-look data, and the SSH issues described above, they can be used as fairly independent measures. As the real-time data are used in the assimilation, one can reasonably expect that the RMSD between the assimilated model and verification data will be consistent with the RMSD between the observational products.

### 3. Data assimilation

Data assimilation is performed via the incremental, strong-constraint four-dimensional variational (IS4DVAR) method described by Courtier et al. (1994) and for the ocean by Weaver et al. (2003). IS4DVAR allows for asynoptic observations to be continuously assimilated using the model dynamics as a constraint. The ROMS IS4DVAR implementation is described in detail by P2008. In IS4DVAR, the goal is to adjust the initial model state,  $\Psi^b(0)$ , to create a time-dependent circulation,  $\Psi(t)$ , that – in a least-squares sense – minimizes the innovation vector,  $\mathbf{d}_i = \mathbf{y}_i - \mathbf{H}_i \Psi^b(t_i)$ .  $\Psi^b(t)$  is the background circulation derived from  $\Psi^b(0)$ ,  $\mathbf{y}_i$  is a vector of observations at individual time  $t_i$ , and  $\mathbf{H}_i$  is an operator that maps the model state vector to the  $i$ -th observation locations. We seek an initial condition,  $\Psi(0) = \Psi^b(0) + \delta\psi$  that minimizes the quadratic cost function:

$$J(\delta\psi) = \frac{1}{2} \delta\psi^T \mathbf{B}^{-1} \delta\psi + \frac{1}{2} \sum_i (\mathbf{G}_i \delta\psi - \mathbf{d}_i)^T \mathbf{O}^{-1} (\mathbf{G}_i \delta\psi - \mathbf{d}_i), \quad (2)$$

where  $\delta\psi$  are perturbations to the initial state,  $\mathbf{B}$  is – in this case univariate – the background error covariance matrix,  $\mathbf{O}$  is the covariance matrix of observation errors and error of representativeness,  $\mathbf{G}_i = \mathbf{H}_i \mathbf{M}$  where  $\mathbf{M}$  represents the integration of the tangent-linear version of ROMS from  $t = (0, t_i)$  linearized about  $\Psi(t)$ .

At the minimum of (2), the gradient  $(\partial J / \partial \delta\psi)$  vanishes and the result,  $\delta\psi_a$ , is the least-squares solution of the data assimilation procedure. Because of the large dimensionality of the problem, the solution  $(\delta\psi_a)$ , is not computed directly, but through a sequence of linear, least-squares minimizations during the “inner-loops” with periodic recalculation of  $\Psi(t)$  in the so-called “outer-loop” to update the circulation about which  $\mathbf{M}$  is linearized. In this implementation, no attempt was made to adjust for uncertainties in the boundary conditions, atmospheric forcing, or model physics. The “representer” method of Bennett (2002) and Chua and Bennett (2001) accounts for these conditions, and is currently implemented in ROMS (Di Lorenzo et al., 2007; Muccino et al., 2008); however, it is not used here.

In this paper, the ROMS IS4DVAR method was extended to use the low-resolution ( $1/3^\circ$ ) model within the “inner-loop” to estimate  $\delta\psi_{10}^a$ , and the higher-resolution ( $1/6^\circ$ ) model is used to generate the non-linear trajectories. In addition, simplifications are required for the linearization of the  $k$ – $kl$  vertical mixing and the surface flux algorithms used in the tangent linear and adjoint models during the inner-loop calculations; otherwise, linear instabilities quickly grow and contaminate



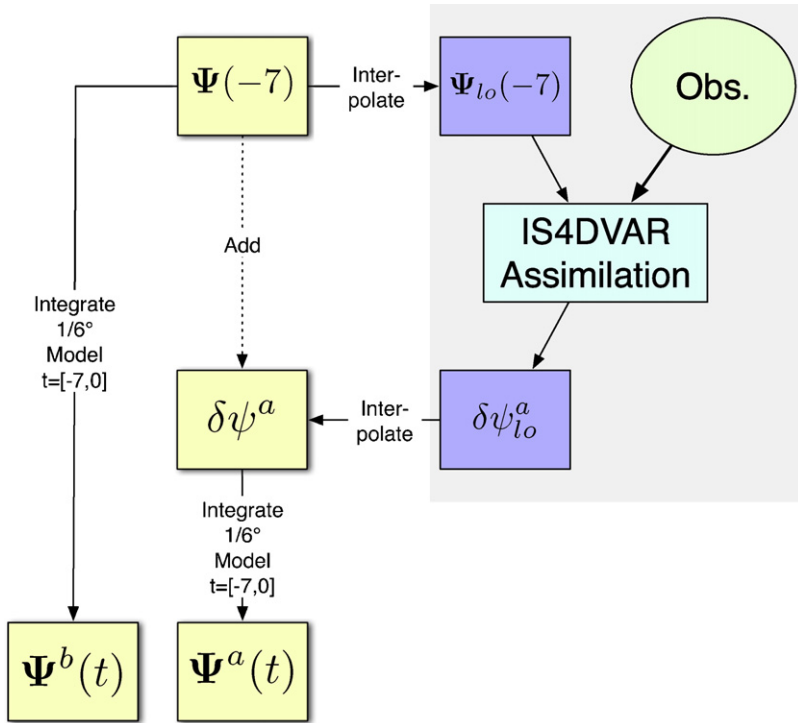


**Fig. 2.** Schematic of the multi-resolution assimilation procedure. A  $1/6^\circ$  first guess estimate from one week prior,  $\Psi(-7)$ , is integrated from  $t = [-7, 0]$  with the higher-resolution model to generate the background field,  $\Psi^b(t)$ , which yields the initial difference between the higher-resolution model and the observations. The first guess is interpolated to the  $1/3^\circ$  model for assimilation. The final, linear increments,  $\delta\psi_{lo}^a$ , are interpolated back to the higher-resolution grid,  $\delta\psi^a$ , and  $\Psi^a(-7) = \Psi(-7) + \delta\psi^a$  is integrated from  $t = [-7, 0]$  with the higher-resolution to generate a nowcast,  $\Psi^a(0)$ .

the solutions. However, the complete  $k$ - $kl$  and COARE algorithms are used in the nonlinear higher-resolution model in the outer-loops. This approach to IS4DVAR where the inner-loop is a lower resolution version of the outer-loop with simplified physical parameterizations is standard practice at some numerical weather prediction centers (Klinker et al., 2000). By reducing the model size and increasing the time-step, the computational benefits of this approach for near real-time assimilation and prediction are clear. We reduced the computational time required for the daily assimilation procedure by a factor of  $\sim 14$ , making it feasible to do near real-time variational assimilation.

The current day (the start of an assimilation/prediction cycle) is denoted as  $t = 0$ . All available data from the previous 7 days  $t = [-7, 0]$  are assimilated into the model to generate a nowcast,  $\Psi(0)$ , as a basis for the ensemble forecast. As shown in Fig. 2, for each cycle, the initial guess is integrated through the nonlinear model to create  $\Psi^b(t)$  where  $t = [-7, 0]$ . The assimilation is performed using 12 inner-loops to compute the linear analysis increments,  $\delta\psi_{lo}^a$ , which are linearly interpolated back to the higher-resolution grid to create  $\Psi^a(-7) = \Psi^b(-7) + \delta\psi^a$ . Integrating  $\Psi^a(-7)$  forward for 7 days using the higher-resolution model yields the nowcast  $\Psi^a(0)$ . This procedure is distinct from P2008 in which only the low-resolution model was used for assimilation.

Each full assimilation and forecasting cycle requires 3 days. As shown in Fig. 3, this yields a 4 days overlap between assimilation cycles, so the previous assimilation circulation estimate provides the first guess for the current assimilation cycle. For each cycle, the nowcast is given by  $\Psi^a(0)$ , the assimilation period by  $\Psi^a(t)$ , where  $t = [-7, 0]$ , and the forecast by  $\Psi^f(t)$ , where  $t = [0, 14]$ .

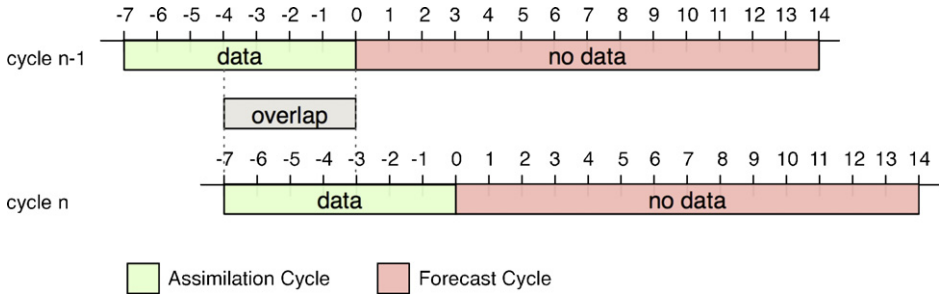


**Fig. 3.** Timeline of the assimilation and prediction cycles performed aboard the *Explorer of the Seas*. During each cycle,  $n$ , all available observations from the preceding 7 days are assimilated into the model to create a nowcast,  $\Psi_n^a(0)$ . Because of the overlap with the previous cycle, the initial guess,  $\Psi_n(-7)$ , is taken from the previous assimilation,  $\Psi_{n-1}^a(-4)$ .

### 3.1. Assimilation statistics

This data assimilation and forecast system was run autonomously for the 7 months duration of the experiment from January 3, 2007 through July 31, 2007 assimilating the near real-time observational data. The initial state estimate was taken from the 2 years assimilation experiment of P2008 on November 20, 2006, was interpolated to the  $1/6^\circ$  model, and the model integrated to January 3, 2007 in order to allow the model to adjust to potential interpolation shocks.

Aggregate statistics over the IAS region (neglecting the portion of the North Atlantic outside of the Antilles island arc as shown in Fig. 1) are used for comparison. The Gulf of Mexico is more active than other regions, and the assimilation performs better in the Caribbean.

Over the 7 months of this experiment, the spatial RMSD mean between the  $1/6^\circ$  model and assimilated real-time observations is found to be 8 cm ( $0.66^\circ\text{C}$ ) for SSH (SST) as shown in Fig. 4. We note that these errors are consistent with the RMSD between the two observational products themselves. This is a reduction of 51% (44%) relative to the RMSD between the observations and the model without assimilation. The RMSD between the  $1/3^\circ$  model used in the inner-loops and the observations is smaller by 11% (21%) versus the higher-resolution outer-loop because the increments minimize the cost function of the lower-resolution model. SSH is subject to the largest difference because the interpolated increments often create inertia-gravity waves that quickly dissipate over 1–2 days. These high-frequency anomalies are due to dynamic imbalances that result from interpolating the increments from the lower-resolution model onto the higher-resolution model.

In P2008, the RMSD mean between the assimilated model and the observations was found to be 4.1 cm ( $0.52^\circ\text{C}$ ) in SSH (SST) for the period from July 2005 through February 2007 using the standard IS4DVAR procedure with the low-resolution model. The present results were derived during a different time-period using the high-resolution model, but the sharp increase in the SSH RMSD illustrates the problem created by the inertia-gravity waves that are introduced in our multiple-resolution assimilation.

The assimilation cycle is repeated every 3 days using observations from the previous 7 days to generate a new circulation estimate. Fig. 3 shows that the previous assimilation provides the initial guess,  $\Psi_{n-1}^a(-4)$ , for the current cycle. This initial guess assimilated data that overlapped with the current cycle, and is integrated to generate the background circulation,  $\Psi^b(t)$ , as in Fig. 2. The overlap period of 4 days in which the same observations are considered during subsequent assimilation cycles allows us to consider  $\Psi^b(t)$  as a 3 days hindcast over the non-overlapping period. Over the interval  $t = [-7, -3]$ ,  $\Psi^b(t)$  should compare favorably to the observations and diverge over the period  $t = (-3, 0]$ , when observations were not available to the previous cycle. As shown in Fig. 4, the hindcast provides an estimate of how quickly the circulation forecast may diverge from the observations over 3 days. For the entire period, the RMSD between the hindcast and observations is 5% (11%) larger in SSH (SST) than the assimilation cycles.



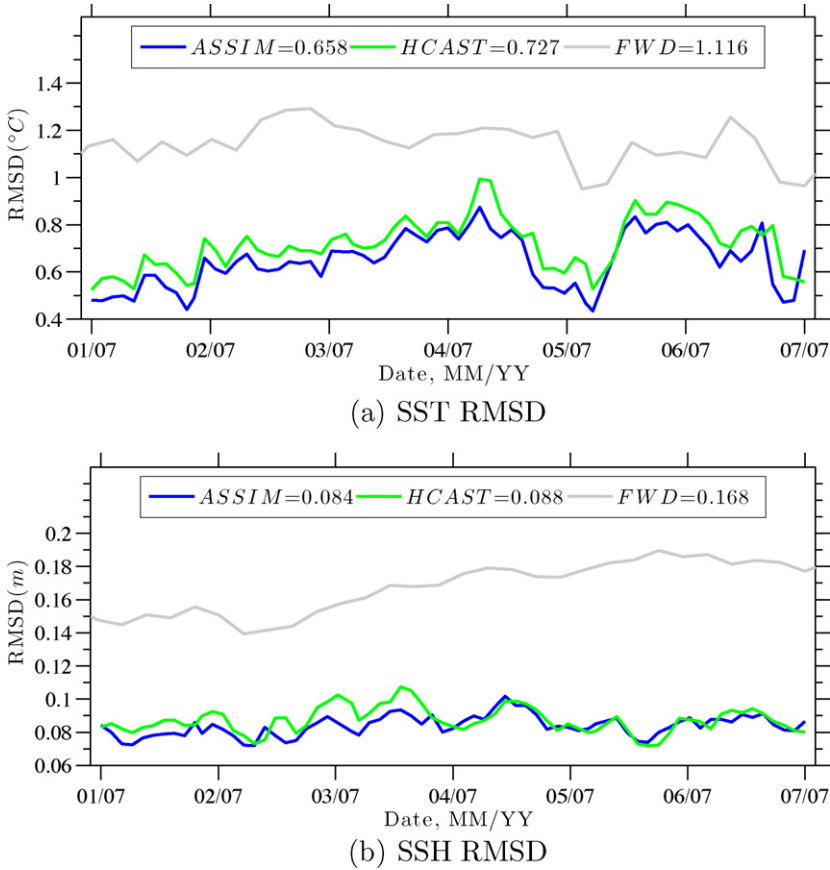


**Fig. 4.** Time series comparing RMSD between the observations and the assimilated solution (ASSIM), the 3 days hindcast (HCAST), and model without assimilation (FWD) for SST and SSH. (a) SST RMSD and (b) SSH RMSD.

The 3 days error growth is consistent with the limit of deterministic predictability. Assuming that the mean squared error increases linearly towards the limit of deterministic predictability, then over 3 days, SSH (SST) will increase by 6.7% (14%) given 45 (21) days to reach the limit. The growth towards the limit of deterministic predictability will be primarily linear for short periods, which explains why the actual prediction error growth compares favorably.

### 3.2. Independent data comparisons

As noted in Section 2.2, the real-time satellite data are capable first-look products but are limited in accuracy by a lack of posterior data and quality controlled observations compared to time delayed validated science data. Using the time-delayed, daily, full-field estimates of Foley-SST and Aviso SSH anomalies a set of verification data was created; however, there were several gaps of Foley-SST data during the experiment.

Similarly, the overlapping, near real-time daily ocean states from the assimilation cycles (which assimilated GHRSSST-PP and CCAR SSH) are combined into “analysis” fields. To remove the seasonal cycle, the monthly SST climatology is subtracted from both the verification and analysis fields to work with the resulting anomalies. The SST climatology was created using 16 years of 4 km resolution Pathfinder v.5 AVHRR SST data (Kilpatrick et al., 2001) from 1990 to 2006. SSH monthly mean dynamic height climatology was computed using a 15 years non-assimilating model run of the 1/6°

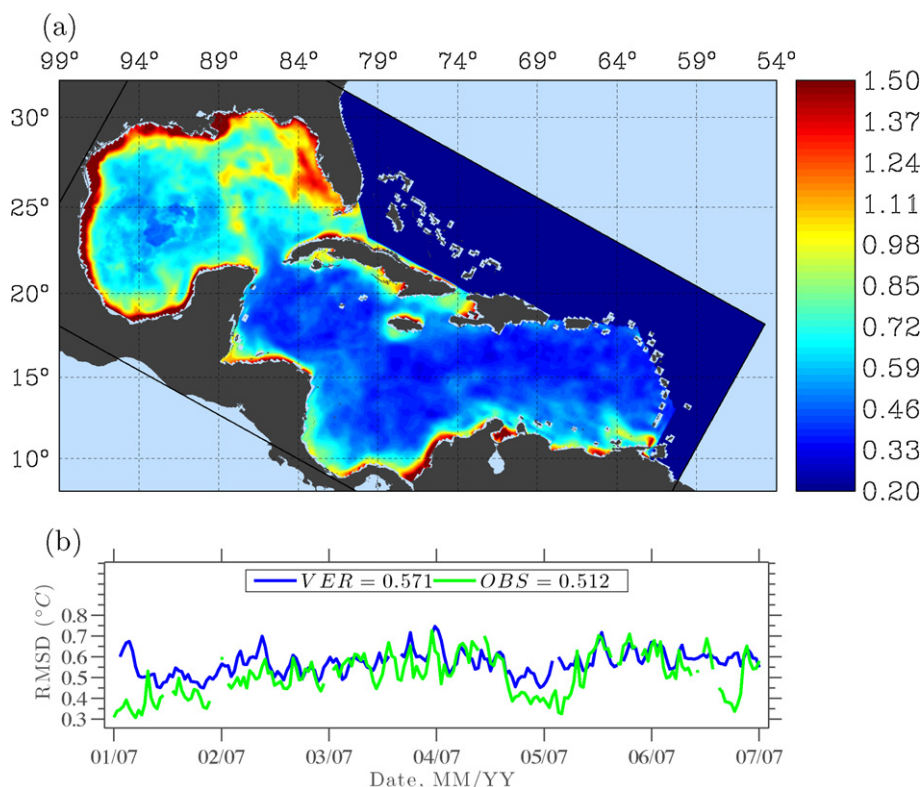


**Fig. 5.** The RMSD between the analysis and verification SST fields in °C. The top panel shows a map of RMSD at each model grid point over time. The bottom panel shows a time series of spatially averaged RMSD between the analysis and verification fields (VER) and between the analysis and observations (OBS).

model, and was subtracted from the analysis field to create model-derived SSH anomalies to compare directly with the Aviso anomalies.

Comparing the analysis SST to the observations in Fig. 5, the time mean of RMSD is found to be slightly lower than in Fig. 4 because combining the overlapping assimilation cycles smooths the analysis field in comparison to the individual assimilation cycles. Fig. 5(a) shows the RMSD between the analysis and verification fields for every model grid-point in time. The RMSD is greatest along the coast where the relatively coarse resolution of the model does not fully resolve the coastal processes and in the vicinity of the dynamically active LC, which is the source of the greatest variability in the GOM. As shown in Powell and Moore (2009), the observations compared to the verification data reveal a similar spatial pattern around the LC, suggesting that the disagreement is between the real-time and delayed products.

The analysis SSH field (Fig. 6) exhibits greater percentage disagreement between the verification data and observations than does SST. The RMSD between the analysis and verification fields is again greatest around the LC, particularly where eddies are likely to separate from the LC. In fact, over the entire region, the RMSD is relatively low but is dominated by the GOM eddy structures. The region near Panama is a spurious signal that was present in the near real-time data but not present in the verification data. Fig. 6(b) shows the time series of spatial RMSD between the analysis and verification fields averages over 10 cm, while the RMSD between the analysis and observations is less than 8 cm. The difference between the analysis and verification fields is consistent with the RMSD between the observation and verification fields. The initial 3-month period of degraded near real-time altimetry data is evident in the time series plot (Fig. 6(b)) where the difference between the verification and

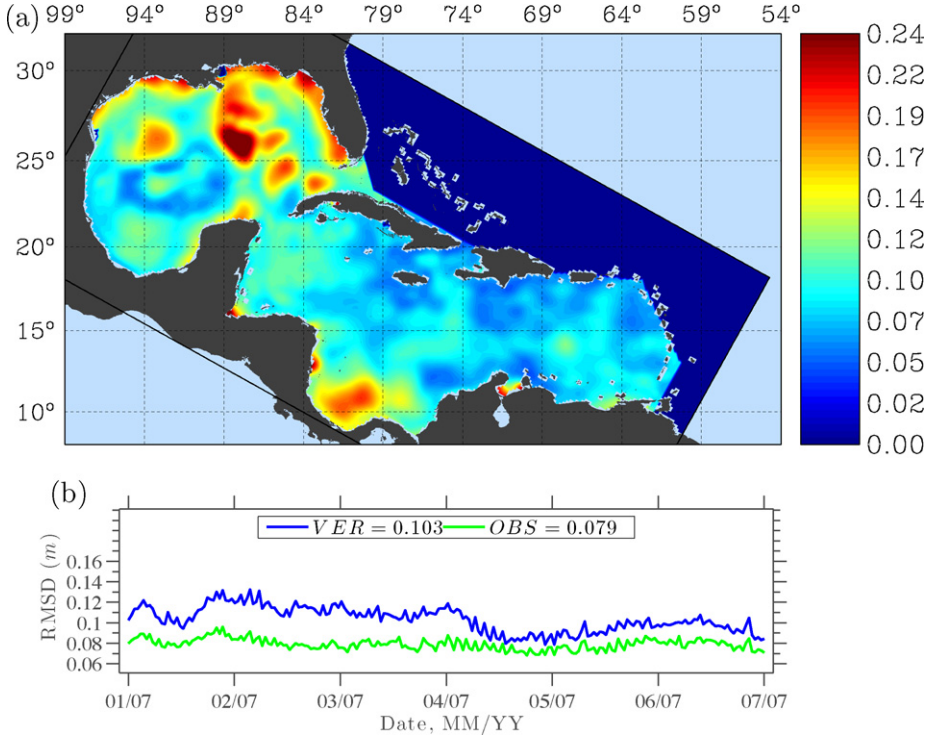


**Fig. 6.** The RMSD between the analysis and verification SSH fields in meters. The top panel shows a map of RMSD at each model grid point over time. The bottom panel shows a time series of spatially averaged RMSD between the analysis and verification fields (VER) and between the analysis and observations (OBS).

observations is greatest. During the first (last) three months, the RMSD between the assimilation and verification fields averages 11.2 (9.5) cm.

The anomaly correlation coefficient (ACC) provides a measure for how well the spatial patterns of SSH and SST correlate between the two fields,  $\mathbf{x}$  and  $\mathbf{y}$ , given by

$$\text{ACC}(\mathbf{x}, \mathbf{y}) = \frac{\sum_{i=1}^n (x_i - \bar{a})(y_i - \bar{a})}{\left[ \sum_{i=1}^n (x_i - \bar{a})^2 \sum_{i=1}^n (y_i - \bar{a})^2 \right]^{(1/2)}}, \quad (3)$$

where  $\bar{a}$  represents the climatological mean field. For SST,  $\bar{a}$  represents the monthly Pathfinder SST mean described in Section 3.2. This presents a difficulty in the analysis because neither the observations, model, nor the verification data are based upon the Pathfinder SST, and the assimilation may push the model closer towards the observations but further from the climatology. In the case of SSH,  $\mathbf{x}$  and  $\mathbf{y}$  are anomalies with  $\bar{a} = 0$ .

Fig. 7 shows the time-series of ACC comparing both the analysis and observation fields to the verification field along with the ACC between the model without assimilation and the verification fields. Neither SSH or SST of the non-assimilating model has any ACC skill compared with the verification data. In SST, the analysis fields have considerably more skill in ACC as compared to SSH; however, the ACC of the analysis compared to the verification data remains around 0.5, the value at which the forecast skill corresponds to the climatology. The reasons for the low ACC values between the model and verification are because the assimilated real-time observations compare quite poorly with the verification data (see “OBS” on Fig. 7), and they limit the ability of the assimilation model to match with the verification. Comparison between the analysis and the observations (not shown) are high with an average above 0.7 (0.8) in SST (SSH). For SSH, the analysis significantly correlates with the

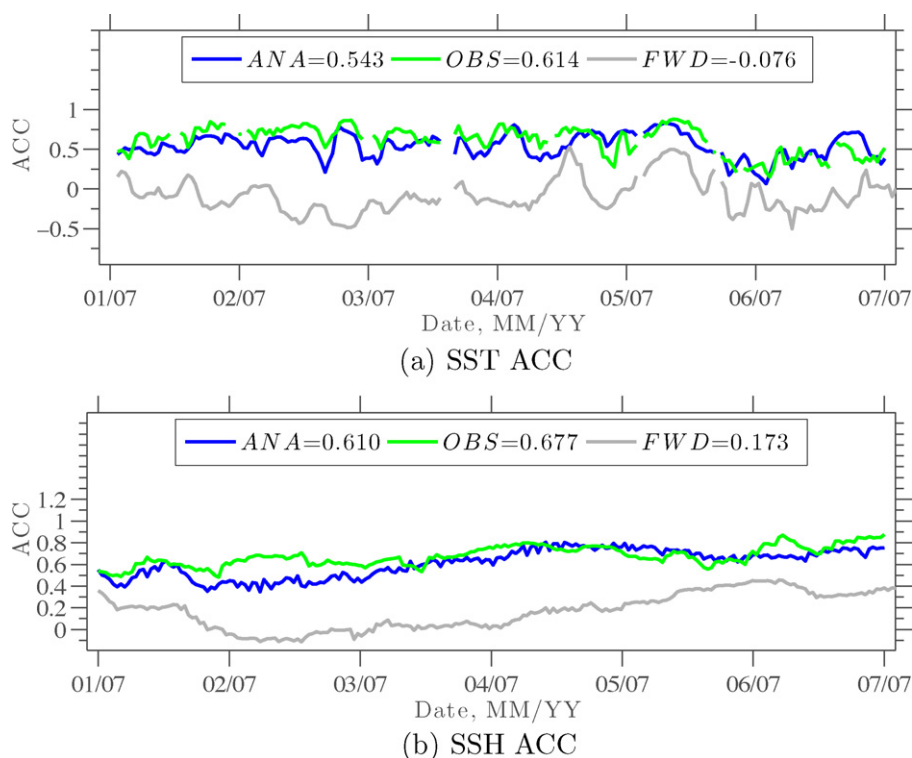


**Fig. 7.** Time series of ACC between the verification and analysis (ANA), observations (OBS), and non-assimilating model (FWD) for the SSH and SST fields. (a) SST ACC and (b) SSH ACC.

observations, but due to the satellite outage during the first 3 months of the experiment, the comparison with the verification is rather poor. The first (last) 3 months have an ACC of 0.48 (0.71). Therefore, the analysis compares poorly with the verification data but the assimilated observations compare just as poorly with the verification data.

The SSH RMSD and ACC results are disappointing and expose two problems with our real-time assimilation: a reliance upon first-look satellite data, and the need for computational efficiency resulting in the use of low resolution models ( $1/3^\circ$  and  $1/6^\circ$ ). The differences in the ACC and RMSD between the analysis and verification fields are similar to the differences between the observation and verification fields. This suggests that no matter how well the model compares with the near real-time data, it cannot be expected to reduce the errors between the observation and verification data. Furthermore, the interpolation of the full field from high to low resolutions and the increment fields back to the higher resolution model introduces dynamical imbalances in the model that result in initialization shocks (Daley, 1991). The imbalances primarily manifest as inertia-gravity waves in the SSH that propagate in the domain for 1–2 days.

Despite these issues, at the end of each 7 days assimilation window, a nowcast is obtained for the current ocean state that has minimized the initial uncertainty (as compared to the observations) and forms the basis for the ensemble forecasts.

#### 4. The ensemble forecast system

Non-linearities in ocean dynamics imply that a sensitive dependence on the initial conditions limit the ability of a forecasting system. Uncertainties and errors in the model representation and the initial state may grow in time and degrade the forecast. Assimilating the observations from the 7 days period

immediately preceding the nowcast has reduced the initial state error. Limited estimates of the initial state error can be obtained from the Hessian matrix generated during the assimilation period (Fisher and Courtier, 1995 and ROMS implementation in Powell and Moore, 2009); however, application of this technique can be computationally expensive, and it was not feasible for the system described here. Monte-Carlo techniques provide a method for sampling nowcast uncertainties, and they form the basis of ensemble forecasting (Leith, 1974).

The primary difficulty in ensemble forecasting is creating a representative sample of the prior probability distribution function (PDF) of the nowcast uncertainty that, once time-integrated, adequately estimates the time posterior PDF. Leutbecher and Palmer (2008) detail a comprehensive method using singular value decomposition to generate a representative sample of the nowcast uncertainty, and this method is used at the European Centre for Medium-Range Weather Forecasting. Similar calculations are possible within ROMS (Moore et al., 2004), but the computational expense of singular value decomposition calculations for each initial flow estimate was prohibitive for this experiment. Therefore, a simplified approach to ensemble generation by utilizing the sequence of increments ( $\delta\psi$ ) generated during the IS4DVAR assimilation procedure is adopted.

#### 4.1. Ensemble generation

During the IS4DVAR assimilation procedure, a nowcast,  $\Psi^a(0)$ , is generated by minimizing the cost function (2) with observations from the previous 7 days using 12 iterations of the conjugate-gradient algorithm. Each iteration creates a state-increment,  $\delta\psi_i$  where  $i = [1, 11]$ , that provides a set of perturbations that can be used to generate an ensemble (note that there are only 11 because  $\delta\psi_0 = 0$ ).

Our aim is to construct a set of independent perturbations, denoted  $\delta\hat{\psi}$ , that approximate a random draw from the uncertainty in our initial-state. If the statistics assumed for  $\mathbf{B}$  and  $\mathbf{O}$  from (2) are a good approximation to the true errors, then the sequence of increments,  $\delta\psi_i$ , generated during the assimilation cycle should be consistent with the assumed errors since the nowcast is a minimum variance (maximum likelihood) estimate. The increments are valid in the Hessian space of Eq. (2), which describes the uncertainty of the nowcast (Powell and Moore, 2009).

Each field increment,  $\delta\psi_i$ , was normalized by the standard deviation of the model field climatology,  $\sigma_{\text{mod}}$ , to create a non-dimensional, scaled increment:  $\delta\omega_i = \delta\psi_i / \sigma_{\text{mod}}$ . A larger sequence of 20 perturbations,  $\delta\hat{\psi}_j$ , is created using random combinations of the orthonormal vectors,  $\delta\omega_i$ , according to  $\delta\hat{\psi}_j = \sum \alpha_i \delta\omega_i$ , where  $j = [1, 20]$  and  $\alpha_i$  is a Gaussian random scalar with a mean of 0 and standard deviation of 1. The choice of 20 perturbations was made to balance the size of the sample and the computational time that would be required to time-integrate each increment. The new increments are rescaled into dimensional space as

$$\delta\hat{\psi}_j = \sigma_{\text{mod}} \delta\hat{\psi}_j = \sigma_{\text{SST}}^2 \left[ (1/N) \sum_{i=1}^N \left( \delta\hat{\psi}_{j(\text{SST}_i)} - \overline{\delta\hat{\psi}_{j(\text{SST})}} \right)^2 \right] \quad (4)$$

where  $\sigma_{\text{SST}}^2$  is the variance of SST in the model climatology and  $N$  are the number of SST points in  $\delta\hat{\psi}_{j(\text{SST})}$ . Because the uncertainty is dominated by the SST assimilation (Powell and Moore, 2009), we scale all increments by the ratio of the climatological variance and the increment's variance.

Eq. (4) yields perturbations with amplitudes that are consistent with those generated by the IS4DVAR procedure—samples from the Hessian space. An ensemble of initial-state estimates was created by both adding and subtracting  $\delta\hat{\psi}_j$  to  $\Psi^a(0)$  and is denoted by  $\Psi_n(0)$ , where  $n = [0, 40]$  and  $\Psi_0(0) = \Psi^a(0)$  (the unperturbed case). The resulting 41 members were integrated forward in time using the 1/6° model for 14 days to generate an ensemble of forecasts. This procedure was repeated for every assimilation and forecast cycle of the experiment.

For a perfect model, the variance of all ensemble members about the ensemble mean should equal the mean squared difference between the ensemble mean and the truth. Denote  $\Psi_n^m(t)$  as the  $n$ th member of the  $m$ th ensemble cycle. Following Leutbecher and Palmer (2008), the spread of the  $m$ th

ensemble is given by

$$s_m^2(t) = \frac{1}{N} \sum_{i=1}^N (\Psi_f^m(t) - \bar{\Psi}_f^m(t))^2, \quad (5)$$

where  $f$  is the field of interest,  $\bar{\Psi}_f^m(t)$  is the ensemble field mean at time,  $t$ . Leutbecher and Palmer (2008) show that for a perfect model, the mean squared error of the ensemble mean,  $\sigma^2$ , and the spread of the ensemble about the ensemble mean,  $s^2$ , should converge as

$$\lim_{M \rightarrow \infty} \frac{1}{M} \sum_{m=1}^M \left( 1 - \frac{N+1}{N-1} \frac{s_m^2}{\sigma_m^2} \right) = 0. \quad (6)$$

From January 2, 2007 through August 11, 2007, 67 ensemble prediction cycles ( $M = 67$ ,  $N = 41$ ) were run. The convergence (6) in SSH (SST) is found to be  $-0.32$  (0.88). Therefore, in SSH, the ensemble spread is over-dispersive (i.e., it is larger than the error in  $\bar{\Psi}^m$ ). As discussed earlier, the dynamical imbalances created by the interpolation from the lower-resolution model onto the higher-resolution model generate inertia-gravity waves in SSH that lead to an over-dispersive ensemble. On the other hand, SST is under-dispersive (the ensemble spread is too small compared to the error in the ensemble mean). A possible contributing factor to the under-dispersion in SST of the ensemble may be due to the atmospheric forcing. The SST is strongly influenced by the heat flux, and both the wind stress and downward radiative fluxes remain unchanged for each ensemble member. Calculating the time scale required to vary the upper model layer (which is used to calculate the SST), anywhere from 3 to 20 days (with most under 14 days) – depending on the region of the domain – are required for the atmospheric forcing to change the SST by 1 °C. Therefore, over a relatively short time, the atmospheric forcing will push the SST field towards a consistent value no matter the perturbations in temperature (and in some cases, the time is shorter than the forecast period). For the prediction cycles, the spread in SST actually decreases over the 14 days prediction period, which would indicate the atmospheric forcing is an issue. An additional problem in SST is shown in Fig. 5(a), which reveals that the major contribution to the RMSD occurs along the shallow shelves, which are poorly resolved by the model, but (6) assumes a perfect model.

#### 4.2. Ensemble forecast results

With an estimate of the initial state from the data assimilation (despite the discrepancy between the near real-time assimilated observations and the truth) and the knowledge that the prediction scale of 14 days is within the limit of deterministic predictability (despite the spread dispersion), the forecasts of SST and SSH are compared with the verification data. The RMSD and ACC between the mean forecast and the verification fields is shown for each day in Figs. 8 and 9.

Each figure shows Hovmöller plots for each assimilation and forecast cycle, and the value for each day of the cycle relative to the day of the nowcast (see Fig. 3). Negative days correspond to the assimilation period and positive days to the forecast period. In each case, blue designates higher skill. In SST, there were numerous data outages during the experimental period, which are shown by the white regions. SST RMSD (Fig. 8(a)) is quite low throughout the assimilation and prediction cycle, which is consistent with Fig. 5. There are some periods (particularly the predictions in mid-May) where strong deviations in the Caribbean appear between the ensemble mean and verification data. In SSH (Fig. 8(b)), the initial period of degraded near real-time SSH observations is evident with high RMSD during both the assimilation and forecast. Once the GFO data was online in April and the Jason-1 stream was updated, the comparison with the verification improved. During the forecasts in mid-June, the assimilated state showed an eddy-shedding event that did not fully separate in the verification field.

Fig. 9(a) exposes the issue of comparing the ACC between the model and truth using an independent climatology to generate the anomalies. Despite a low RMS between the two fields, there is little apparent model skill in ACC. Comparing the observations with the verification fields (not shown) reveals a similar pattern, further suggesting that the poor ACC skill is due to the reliance on near real-time



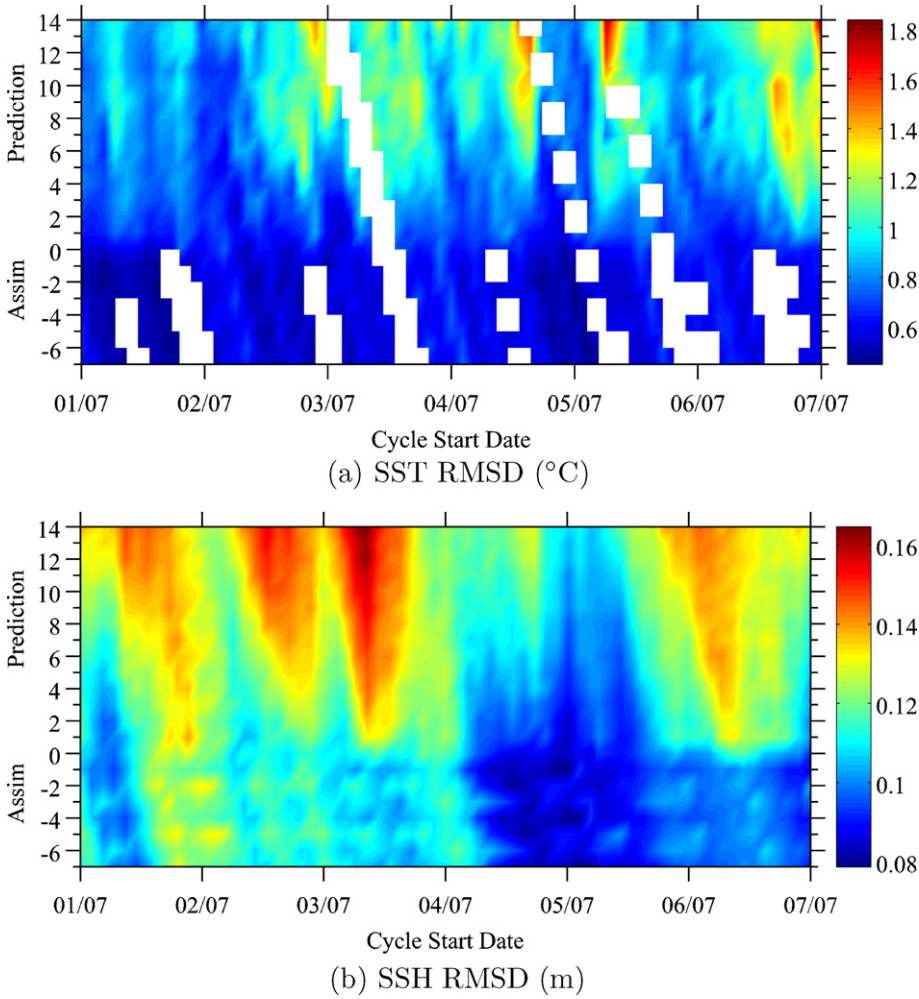


**Fig. 8.** Hovmöller plots of RMSD between the ensemble mean and verification fields for each day of every assimilation/forecast cycle. Negative (positive) times indicate the assimilation (forecast) period. Blue values indicate higher skill in RMSD. (a) SST RMSD ( $^{\circ}\text{C}$ ) and (b) SSH RMSD (m).

observations. The choice of a separate climatology based upon the verification data would be ideal; however, the time period for which verification data are available is too short. SSH ACC (Fig. 9(b)) is very similar to the RMSD revealing the degraded nowcast and the incorrect eddy shedding event in late June, which the near real-time observations also showed as a separation event.

As discussed in Section 2.1, a persistence forecast is a benchmark that is often used to gauge the success of a forecast member. In this case, real-time persistence forecasts can only be made using the near real-time observational products. As a result, the persistence forecasts will not be error free on day 0 when compared to the verification data. RMSD and ACC between the current near real-time observations and the verification data are computed as measures of the errors in the persistence forecasts.

Fig. 10 shows the average RMSD between each of the 67 ensemble mean forecasts and the verification data versus forecast day. The shaded region encompasses 90% of the ensemble mean forecasts (i.e., the ensemble means that lie between the 5th and 95th percentile of the ensemble mean forecast

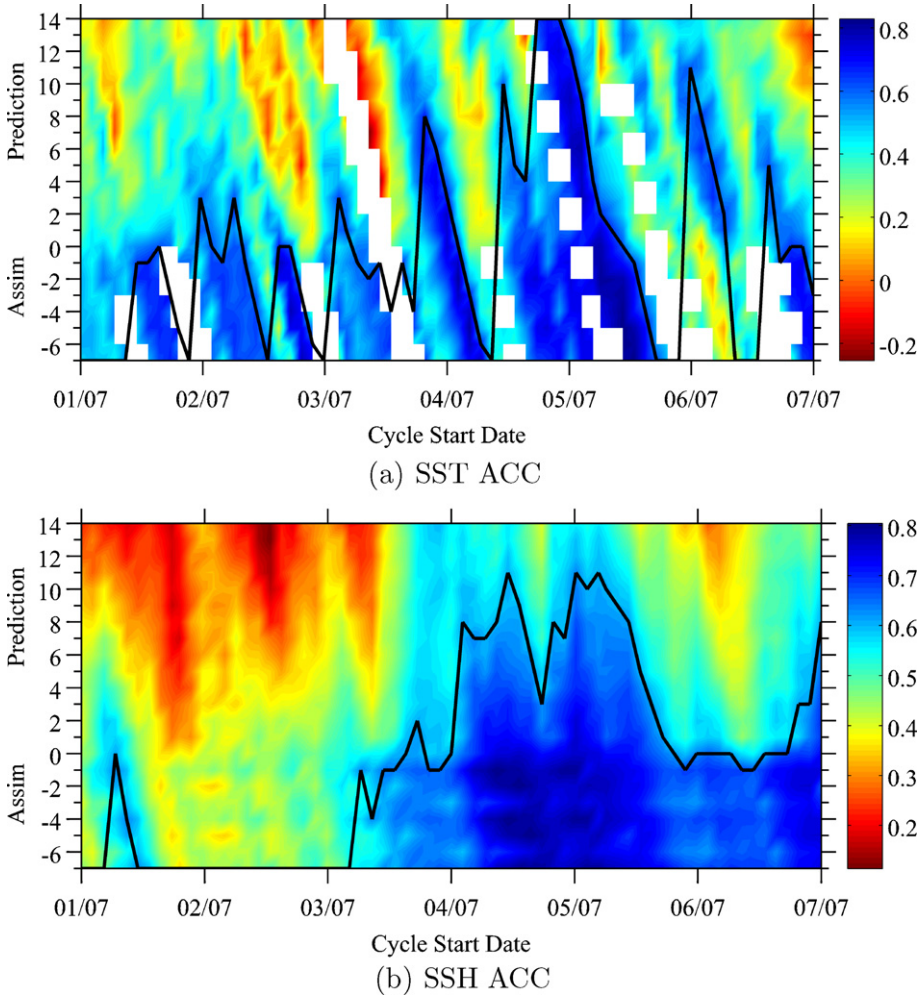


**Fig. 9.** Hovmöller plots of ACC between the ensemble mean and verification fields for each day of every assimilation/prediction cycle. The black line highlights the 0.6 correlation level. Blue values indicate higher skill of ACC. (a) SST ACC and (b) SSH ACC.

distribution). The RMSD for the persistence forecast is shown in red, and the blue, dashed line denotes the limit of deterministic predictability. The nowcast RMSD from the assimilation is consistent with Figs. 5 and 6 for SSH and SST, respectively. In SST, the RMSD grows linearly – on average – by 55% over the 14 days prediction periods, and it is slightly worse than the persistence. Similar to Fig. 5, the largest errors in both SSH and SST are in the vicinity of the LC. On average, the error in SSH grows by 23% over the 14 days period. If the growth towards the limit of deterministic predictability is linear, the SSH (SST) error should grow by 31% (77%).

The ACC shown in Fig. 11 reveals that – on average – the ensemble mean has low skill in the anomaly correlation with the truth. The nowcast begins at values consistent with climatology (0.5 ACC value), as shown in Fig. 7. The poor correlation between the nowcast and the verification data reiterates the limitation of relying on near real-time surface satellite products for assimilation, and the difficulty of using an independent climatology. For SST, the ensemble mean does not – on average – beat persistence, but the 95th percentile shows that for some prediction cycles, the ensemble mean forecast is significantly better. Fig. 11(b) shows that for SSH, the average mean forecast is similar to

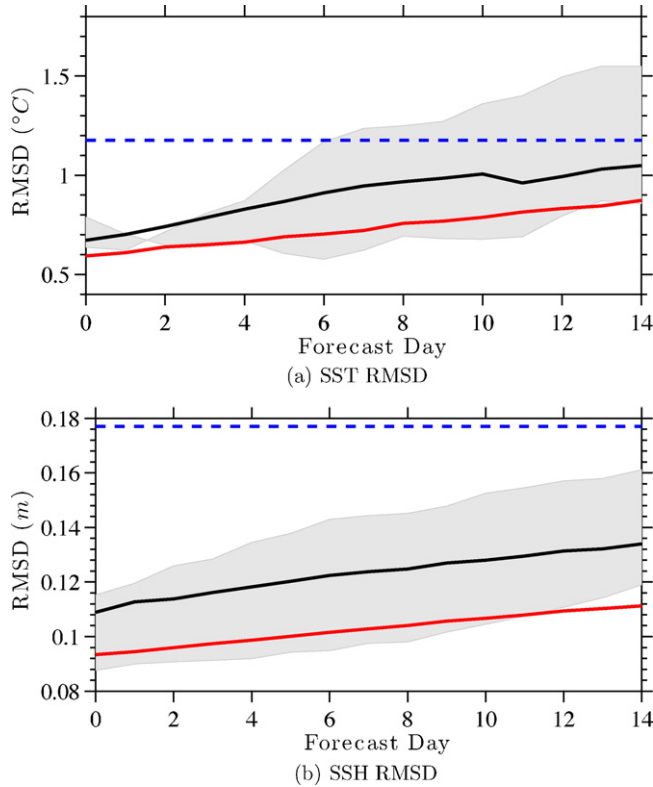


**Fig. 10.** Time series of SST and SSH RMSD for all ensemble mean forecasts compared to the verification data. The average ensemble mean forecast is shown in black with the shaded region bounded by the 5th and 95th percentile of ensemble means. The RMSD between persistence and the verification data is shown in red and the limit of deterministic predictability is shown in blue. (a) SST RMSD and (b) SSH RMSD.

persistence, while again the 95th percentile reveals that there are periods where the ensemble mean is significantly better than persistence.

The time dependent values of ACC for the ensemble mean forecast and the 5th and 95th percentiles on day 14 for each assimilation/forecast cycle are shown in Fig. 12 along with ACC for persistence. The SST shows evidence of the collapse of the SST spread due to the consistent atmospheric forcing between ensemble members with little difference between the mean, 5th and 95th percentile cases. Over the entire 7 months period, persistence generally beats the prediction system for SST except during the summer season when the model performs better. Choosing the skill on day 7 rather than 14, Fig. 11 shows that the 95th percentile ensemble mean member is significantly better than persistence. Once the early near real-time SSH observation issues were resolved, the model was consistently superior to persistence (Fig. 12(b)), and the day 14 spread is large; however, all values remain below 0.6 suggesting there is no significant skill. As shown in Fig. 11(b), neither the near real-time observations or the nowcast has any skill in ACC, so the forecast cannot be expected to improve upon it.

#### 4.3. Forecasting Circulation Features

The near real-time observations – along with the assimilated nowcast and their derived forecasts – have poor skill against the verification data for aggregates of the region. In this section, we attempt to elucidate the capability of the forecasts in predicting LC intrusion and LC eddies. The effect of LC and/or warm eddies on hurricane intensification has been well documented in studies of the rapid

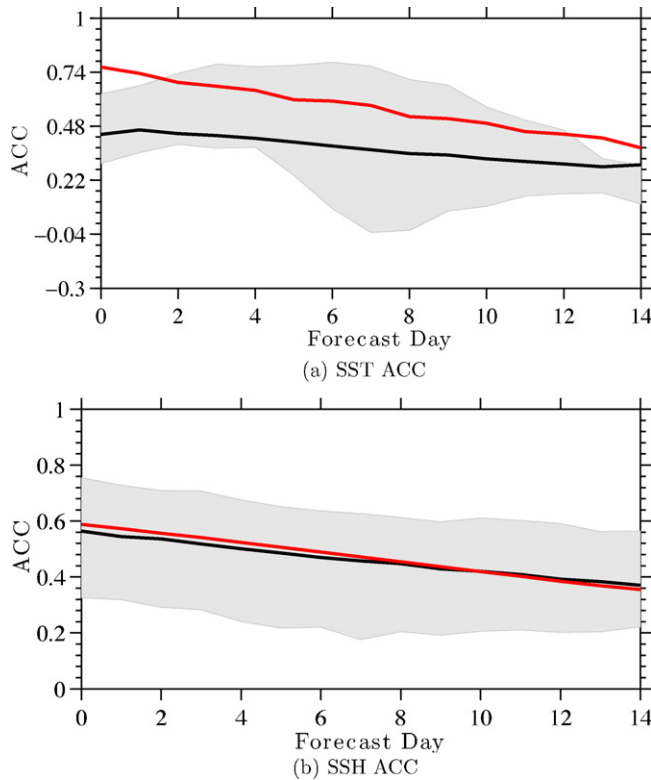


**Fig. 11.** Time series of SST and SSH ACC for all ensemble mean forecasts compared to the verification data. The average ensemble mean forecast is shown in black with the shaded region bounded by the 5th and 95th percentile of ensemble means. The ACC between persistence and the verification data is shown in red. (a) SST ACC and (b) SSH ACC.

intensification of Hurricane Opal over a Loop Current eddy in 1995 (Shay et al., 2000) and the interaction of Typhoon Maemi with a warm ocean eddy in the Northwest Pacific in 2003 (Lin et al., 2005). Both Katrina and Rita crossed the warm waters of the intruded Loop Current and Eddy Vortex, contributing to the marked increases in the maximum sustained wind speeds over those features. When accurate upper ocean eddy heat content information is incorporated into coupled atmosphere/ocean prediction systems the estimates of hurricane intensity are improved (Emanuel and Rodríguez, 2004).

Leben (2005) developed a set of indices for the LC, which are adopted to derive an estimate of the maximum northern latitude of the LC during each forecast cycle. A reliable forecast of the northern intrusion of the LC provides valuable information on the current state of the LC. Fig. 13 shows the time-series of maximum northern latitude for the LC from day 14 of each forecast cycle. The ensemble mean forecast is in black with the shaded region bounded by the 5th and 95th percentile ensemble members. Similarly, the maximum latitude is shown for the near real-time observations and the verification data with their associated errors. During the early part of the experiment, when the near real-time SSH was experiencing difficulties, the maximum latitude was underestimated as estimated by the verification data. Around the beginning of April, once the near real-time data had been corrected, the forecast maximum latitude was consistent with the verification data. For most of the series, there were ensemble members that were within the range of the verified data; although, many members seemed to intrude too far north.

Anticyclonic LC eddies separate from the LC at irregular intervals with diameters between 150 and 500 km and a westward propagation speed of  $1\text{--}3\text{ km day}^{-1}$  (Glenn and Ebbesmeyer, 1993; Hamilton et al., 1999). In December 2006, a large LC eddy detached from the LC, and we tracked its progress using

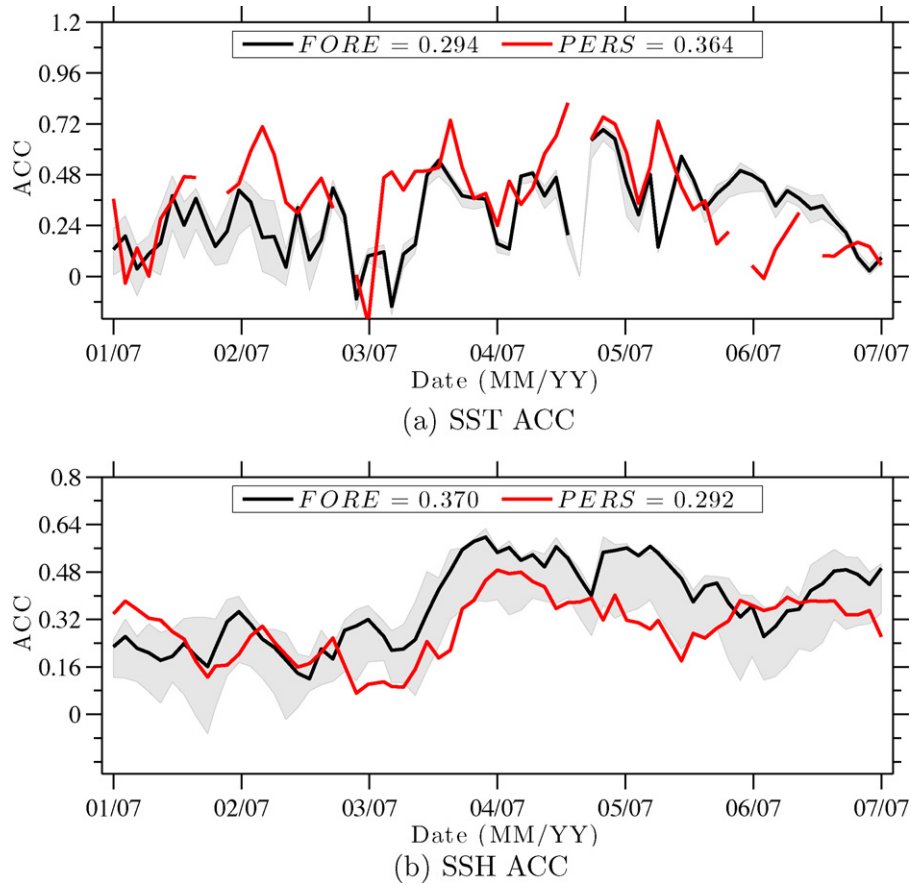


**Fig. 12.** Time series of SST and SSH ACC between the ensemble mean forecast (FORE, in black) and verification data on the 14th day of the forecast with the 5th and 95th percentile bounding the shaded region. ACC between persistence and the verification data is shown in red (PERS). (a) SST ACC and (b) SSH ACC.

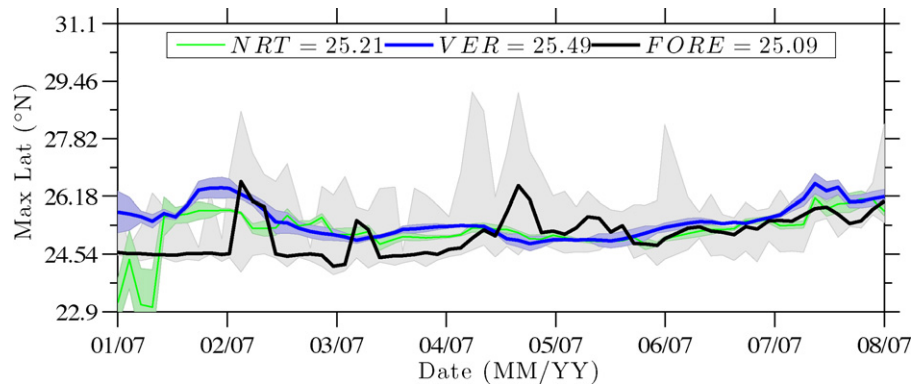


**Fig. 13.** Time series of maximum northern latitude of Loop Current intrusion into the GOM on day 14 of the forecast. Latitude derived from the near real-time observations is shown in green with the verification data (VER) in blue. Both are bounded by their respective standard deviation. The ensemble mean forecast (FORE) is shown in black with the grey region bounded by the 5th and 95th percentile ensemble forecast members.



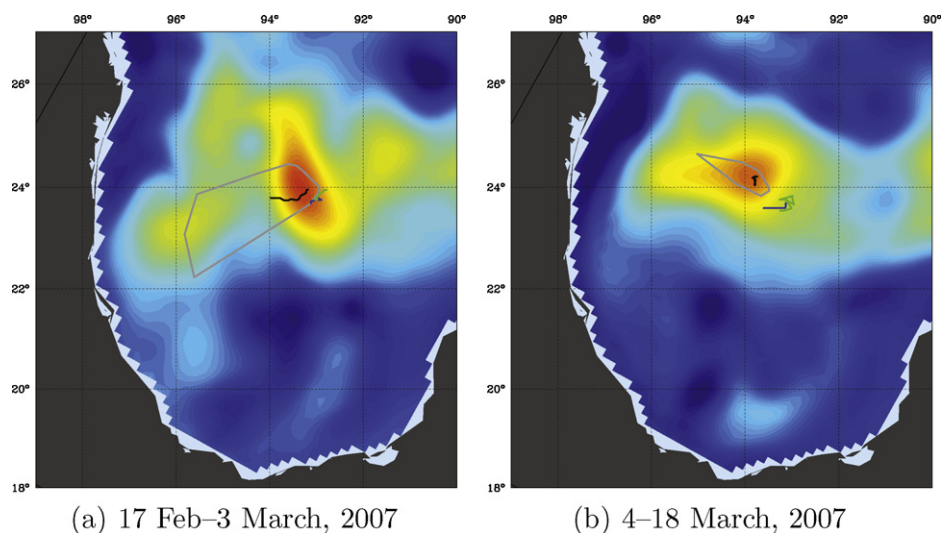


**Fig. 14.** Locations of forecast eddy center positions during two forecast periods overlaying the nowcast SSH field. The forecast date and (nowcast date) are shown. The black line shows the trajectory of the eddy center from the ensemble mean forecast and the grey area bounds the range of the ensemble members. After the forecast, the path as determined by the near real-time observations (green) and the verification data (blue) are shown. The 3 March case is one of the better forecasts, and the 18 March case is one of the worst. (a) 17 February–3 March, 2007, (b) 4–18 March, 2007.

the data from the ensemble forecasts, real-time observations, and verification observations. From Feb. through March, we compared the location of the eddy center between each ensemble forecasting cycle with the observational data.

Fig. 14 shows two cases of the predicted eddy paths over two forecast periods. Each figure shows the initial SSH field overlaid with the ensemble spread of the predicted eddy center over 14 days in grey, the ensemble mean forecast in black, and the paths derived from the subsequent near real-time observations (green) and the verification data (blue). In each case, the eddy location is not collocated with the observations (as suggested by the poor ACC skill). The initial case (Fig. 14(a)) from 17 February through 3 March, the ensemble spread covers the path calculated from the observations and verification; however, the propagation speed is too rapid. It appears that the eddy tracking algorithm may have been confused by the second, smaller eddy to the west. Later in the month (Fig. 14(b)), the model transported the eddy westward, while both the observations and verification show the eddy core nearly in the same place as during the earlier period. As both the observation and verification data show a similar eddy center, it appears that the assimilated nowcast has the eddy in the wrong location and the ensemble starts from the incorrect location.

## 5. Conclusions

This experiment served as a proof-of-concept for implementing an assimilation and forecasting system with an autonomous, stand-alone machine onboard a ship of opportunity based upon numerical weather prediction. Although there was diminished skill as compared to persistence, the model remained consistent with the near real-time observations used in the assimilation. The surface forecast skill of the assimilated solutions was shown (Fig. 4) to be greater than the non-assimilated solutions. Because the variational method constrains the assimilation with the model dynamics, assimilation of the surface fields also dynamically reduces the uncertainty in the subsurface fields Powell and Moore (2009). With improved surface and subsurface forecasts, the ensemble forecasts should have more value than surface observational persistence, but this requires further study. Despite the overall lack of predictive skill, the forecast model was able to provide reasonable forecasts of the LC intrusion. Quick-look near real-time observations may be the primary weakness to any real-time system due to their significant differences with the posterior, science-quality processed observations.



The feasibility of a future system will rely upon improvements made to each of the following issues:

- (i) The poor representation of shelf physics in the domain could be improved (along with other dynamical issues) by increasing the resolution of the model.
- (ii) The addition of the inertia-gravity waves from the interpolation between model resolutions could be reduced or removed by including an additional constraint term in (2). In this experiment, this spurious energy was not suppressed; however, we are working to add a digital filter to (2) that would suppress this energy (Gauthier and Thépaut, 2001).
- (iii) There are two issues with the atmospheric forecasts used for forcing the model: the accuracy of the forecast and the use of a single forecast to force all ensemble members. We cannot control the accuracy of the atmospheric forecast; however, there are methods that could be used to perturb the atmospheric forecast to force each ocean ensemble member independently which would allow the spread in SST to grow. Milliff et al. (in preparation) and Bonazzi (2008) have developed a method for generating an ensemble of surface wind fields obtained from the posterior distribution of a Bayesian Hierarchical Model (BHM). Advantages of this approach include computational efficiency and the prospect for generating consistent perturbations in the nowcast fields. Another method is to utilize the differences between forecasts generated by different numerical weather prediction centers (Daget, 2006a, b, 2009).
- (iv) Using the perturbations created during the assimilation procedure as a basis for sampling the nowcast uncertainty provided an efficient method; however, no effort was made to insure that these perturbations were sufficiently better than purely random samples. The uncertainty in the nowcast is given by the inverse Hessian matrix of (2), and the perturbations come from the Hessian sub-space. However, the spread of the ensemble was typically found to be under-dispersive. Under-dispersive spreads can also be a problem in statistical ensemble based schemes (Houtekamer and Mitchell, 1998; Kleeman, 2007).
- (v) The reliance on mapped, near real-time observations was shown to be the primary limiting factor in the comparison between the model and the verification data. The model compared very favorably with the near real-time observations; however, due to the intrinsic differences between the near real-time observations and the verification data, the model could only compare as well as between the two observational sets. Future systems may be better served by relying upon along-track data derived in real-time from each satellite. Although this will not be an improvement over the measurements used in the near real-time observational products, it will prevent the aliasing problems present in the near real-time mapped products, as well as differences in the processing used to generate each product.

Despite some of these issues, there were successes with the experiment including the autonomous capabilities of the system, the dual model resolution method used to increase the efficiency of the data assimilation, an application of using the assimilation perturbations for ensemble generation, and the relative success of the prediction system limited by the near real-time observations from which the forecasts were based.

For this prediction system, we have addressed the influences of uncertainties in physical representation with an advanced regional ocean model, uncertainties in the nowcast with state-of-the-art 4DVAR assimilation, and growth of model-state errors using an ensemble prediction sample. Despite limited resources, we were able to bring these complex systems together that in near real-time was able to occasionally beat persistence and provide a number of possible forecast states over the region.

## Acknowledgements

The authors gratefully acknowledge that this research was supported by ONR grants N00014-05-M-0081, N00014-01-1-0209, N00014-05-M-0275, N00014-05-1-0277, N00014-05-1-0365, and N00014-06-1-0406. Atmospheric forcing was provided by the NOAA/National Centers for Environmental Prediction (NCEP)/Environmental Modeling Center (EMC)/NOMADS development group.

We thank the anonymous reviewers for their thorough and helpful suggestions.

The authors wish to thank Jan Morzel of NWRA, Colorado Research Associates Division, Boulder, CO for his help and support processing a variety of data for this experiment. We thank Elizabeth Williams, Lisa Beal, Warner Baringer, Don Cucchiara, Chip Maxwell, and Otis Brown at the University of Miami, Rosenstiel School of Marine and Atmospheric Sciences (RSMAS). The authors are indebted to the work of David Foley generating the SST fields used as the “truth” comparisons. Finally, Steve Worley of NCAR DSS for facilitating the retrieval of the NCEP 16 day forecast fields.

## References

- Bender, M.A., Ginis, I., 2000. Real-case simulations of hurricane–ocean interaction using a high-resolution coupled model: effects on hurricane intensity. *Mon. Weather Rev.* 128, 917–946.
- Bender, M.A., Ginis, I., Tuleya, R., Thomas, B., Marchok, T., 2007. The operational GFDL coupled hurricane–ocean prediction system and a summary of its performance. *Mon. Weather Rev.* 135, 3965–3989.
- Bennett, A.F., 2002. *Inverse Modeling of the Ocean and Atmosphere*. Cambridge Univ. Press.
- Bonazzi, A., 2008. Ensemble forecasting in the Mediterranean Sea. Ph.D. Thesis. University of Bologna.
- Buizza, R., Barkmeijer, J., Palmer, T.N., Richardson, D.S., 2000. Current status and future developments of the ECMWF Ensemble Prediction System. *Meteorol. Appl.* 7, 163–175.
- Chassignet, E.P., Hurlburt, H.E., Martin Smedstad, O., Barron, C.N., Ko, D.S., Rhodes, R.C., Shriver, J.F., Wallcraft, A.J., Arnone, R.A., 2005. Assessment of data assimilative ocean models in the Gulf of Mexico using ocean color. In: Sturges, W., Lugo-Fernandez, A. (Eds.), *Circulation in the Gulf of Mexico: Observations and Models*, vol. 161. American Geophysical Union, pp. 165–180.
- Chassignet, E.P., Hurlburt, H.E., Martin Smedstad, O., Halliwell, G.R., Hogan, P.J., Wallcraft, A.J., Baraille, R., Bleck, R., 2007. The HYCOM (HYbrid Coordinate Ocean Model) data assimilative system. *J. Mar. Syst.* 65, 60–83.
- Chassignet, E.P., Verron, J. (Eds.), 2006. *Ocean Weather Forecasting: An Integrated View of Oceanography*. Springer-Verlag.
- Chua, B.S., Bennett, A.F., 2001. An inverse ocean modeling system. *Ocean Model.* 3, 137–165.
- Courtier, P., Thépaut, J.-N., Hollingsworth, A., 1994. A strategy for operational implementation of 4D-Var, using an incremental approach. *Q. J. R. Meteorol. Soc.* 120, 1367–1387.
- Daget, N., 2006a. Interpolation d'une grille ORCA2 vers une grille régulière. Tech. Rep. TR/CMGC/06/18, Cerfacs.
- Daget, N., 2006b. Utilisation d'un filtre récursif 1D pour corrélér les perturbations de la SST. Tech. Rep. TR/CMGC/06/17, Cerfacs.
- Daget, N., Weaver, A.T., Balmaseda, M.A., 2009. Ensemble estimation of background-error variances in a three-dimensional variational data assimilation system for the global ocean. *Q. J. R. Meteorol. Soc.* doi:10.1002/qj.412.
- Daley, R., 1991. *Atmospheric Data Analysis*. Cambridge Univ. Press.
- Di Lorenzo, E., Moore, A.M., Arango, H.G., Cornuelle, B.D., Miller, A.J., Powell, B.S., Chua, B.S., Bennett, A.F., 2007. Weak and strong constraint data assimilation in the inverse Regional Ocean Modeling System (ROMS): development and application for a baroclinic coastal upwelling system. *Ocean Model.* 16, 160–187.
- Donlon, C., Robinson, I., Casey, K.S., Vazquez-Cuervo, J., Armstrong, E., Arino, O., Gentemann, C., May, D., LeBorgne, P., Piollé, J., Barton, I., Beggs, H., Poulter, D.J.S., Merchant, C.J., Bingham, A., Heinz, S., Harris, A., Wick, G., Emery, B., Minnett, P., Evans, R., Llewellyn-Jones, D., Mutlow, C., Reynolds, R.W., Kawamura, H., Rayner, N., 2007. The Global Ocean Data Assimilation Experiment High Resolution Sea Surface Temperature Pilot Project. *Bull. Am. Meteorol. Soc.* 88 (8), 1197–1213.
- Donlon, C. J., 2006. The Global Ocean Data Assimilation Experiment High Resolution Sea Surface Temperature Pilot Project (GHRST-PP) Data Processing Specification Version 1.7 (GDSv1.7). Tech. rep., GODAE Project Office, UK Met Office.
- Emanuel, K.A., Rodríguez, E., 2004. High-resolution measurement of ocean surface topography by radar interferometry for oceanographic and geophysical applications. In: Sparks, R.S.J., Hawkesworth, C.J. (Eds.), *AGU Monograph 150. IUGG: State of the Planet: Frontiers and Challenges*, vol. 19, pp. 209–224.
- Fairall, C.W., Bradley, E.F., Rogers, D.P., Edson, J.B., Young, G.S., 1996. Bulk parameterization of air–sea fluxes for tropical ocean–global atmosphere coupled-ocean atmosphere response experiment. *J. Geophys. Res.* 101, 3747–3764.
- Fisher, M., Courtier, P., 1995. Estimating the covariance matrices of analysis and forecast error in variational data assimilation. Tech. Rep. 220. European Centre for Medium-Range Weather Forecasts.
- Gauthier, P., Thépaut, J.-N., 2001. Impact of the digital filter as a weak constraint in the preoperational 4DVAR assimilation system of Météo-France. *Mon. Weather Rev.* 129, 2089–2102.
- Glenn, S.M., Ebbesmeyer, C.C., 1993. Drifting buoy observations of a loop current anticyclonic eddy. *J. Geophys. Res.* 98, 20105–20120.
- Haidvogel, D.B., Arango, H., Budgell, W.P., Cornuelle, B.D., Curchitser, E., Di Lorenzo, E., Fennel, K., Geyer, W.R., Hermann, A.J., Lanerolle, L., Levin, J., McWilliams, J.C., Miller, A.J., Moore, A.M., Powell, T.M., Shchepetkin, A.F., Sherwood, C.R., Signell, R.P., Warner, J.C., Wilkin, J., 2008. Ocean forecasting in terrain-following coordinates: formulation and skill assessment of the Regional Ocean Modeling System. *J. Comp. Phys.* 227, 3595–3624.
- Haidvogel, D.B., Arango, H.G., Hedstrom, K., Beckmann, A., Malanotte-Rizzoli, P., Shchepetkin, A.F., 2000. Model evaluation experiments in the North Atlantic Basin: simulations in nonlinear terrain-following coordinates. *Dyn. Atmos. Oceans* 32, 239–281.
- Hamilton, P., Fargion, G.S., Biggs, D.C., 1999. Loop current eddy paths in the western Gulf of Mexico. *J. Phys. Oceanogr.* 29, 1180–1207.
- Houtekamer, P.L., Mitchell, H.L., 1998. Data assimilation using an ensemble Kalman Filter technique. *Mon. Weather Rev.* 126, 796–811.
- Kalnay, E., Lord, S.J., McPherson, R.D., 1998. Maturity of operational numerical weather prediction: medium range. *Bull. Am. Met. Soc.* 79, 2753–2769.
- Kilpatrick, K.A., Podesta, G.P., Evans, R., 2001. Overview of the NOAA/NASA Advanced Very High Resolution Radiometer Pathfinder algorithm for sea surface temperature and associated matchup database. *J. Geophys. Res.* 106, 9179–9197.
- Kleeman, R., 2007. Statistical predictability in the atmosphere and other dynamical systems. *Physics D* 230, 65–71.

- Klinker, E., Rabier, F., Kelly, G., Mahfouf, J.-F., 2000. The ECMWF operational implementation of four-dimensional variational assimilation. III: Experimental results and diagnostics with operational configuration. *Q. J. R. Meteorol. Soc.* 126, 1191–1215.
- Ko, D.S., Martin, P.J., Rowley, C.D., Preller, R.H., 2007. A real-time coastal ocean prediction experiment for mrea04. *J. Marine Syst.*
- Le Dimet, F., Talagrand, O., 1986. Variational algorithms for analysis and assimilation of meteorological observations: theoretical aspects. *Tellus* 38A, 97–110.
- Leben, R.R., 2005. Altimeter-derived Loop Current metrics. In: Sturges, W., Lugo-Fernandez, A. (Eds.), *Circulation in the Gulf of Mexico: Observations and Models*, vol. 161. American Geophysical Union, pp. 181–201.
- Leben, R.R., Born, G.H., Engebret, B.R., 2002. Operational altimeter data processing for mesoscale monitoring. *Mar. Geodesy* 25, 3–18.
- Lee, T.N., Johns, W.E., Zantopp, R.J., Fillenbaum, E.R., 1996. Moored observations of western boundary current variability and thermohaline circulation at 26.5°N in the subtropical North Atlantic. *J. Phys. Oceanogr.* 26, 962–983.
- Leith, C.E., 1974. Theoretical skill of Monte-Carlo forecasts. *Mon. Weather Rev.* 102, 409–418.
- Leutbecher, M., Palmer, T.N., 2008. Ensemble forecasting. *J. Comp. Phys.* 227, 3515–3539.
- Levitus, S., Burgett, R., Boyer, T., 1994. *World Ocean Atlas 1994*, vol. 4: Temperature. NOAA Atlas NESDIS 4. U.S. Department of Commerce, 132 pp.
- Lewis, J.M., 2005. Roots of ensemble forecasting. *Mon. Weather Rev.* 133, 1865–1885.
- Lin, I.I., Wu, C.C., Emanuel, K.A., Lee, I.H., Wu, C.R., Pun, I.F., 2005. The interaction of Supertyphoon Maemi (2003) with a warm ocean eddy. *Mon. Weather Rev.* 133, 2635–2649.
- Metzger, E.J., Hurlburt, H.E., Wallcraft, A.J., Chassignet, E.P., Cummings, J.A., Smedstad, O.M., 2008. Global Ocean Prediction Using HYCOM, HPCMP Users Group Conference, pp. 271–274.
- Milliff, R.F., Bonazzi, A., Wikle, C.K., Pinardi, N., Berliner, L.M., in preparation. A Bayesian Hierarchical Model to generate ensemble ocean initial conditions for the Mediterranean Forecast System.
- Mooers, C.N.K., Maul, G.A., 1998. Intra-Americas Sea circulation. In: Robinson, A.R., Brink, K.H. (Eds.), *The Sea*. John Wiley & Sons, pp. 183–208 (Chapter 11).
- Moore, A.M., Arango, H.G., Lorenzo, E.D., Cornuelle, B.D., Miller, A.J., Neilson, D.J., 2004. A comprehensive ocean prediction and analysis system based on the tangent linear and adjoint of a regional ocean model. *Ocean Model.* 7, 227–258.
- Muccino, J.C., Arango, H.G., Bennett, A.F., Chua, B.S., Cornuelle, B.D., Di Lorenzo, E., Egbert, G.D., Haidvogel, D., Levin, J.C., Luo, H., Miller, A.J., Moore, A.M., Zaron, E.D., 2008. The Inverse Ocean Modeling System. Part II: Applications. *J. Atmos. Oceanic Technol.* 25, 1623–1637.
- Ohlmann, J.C., Niiler, P.P., Fox, C.A., Leben, R.R., 2001. Eddy energy and shelf interactions in the Gulf of Mexico. *J. Geophys. Res.* 106, 2605–2620.
- Pinardi, N., Woods, J. (Eds.), 2002. *Ocean Forecasting: Conceptual Basis and Applications*. Springer-Verlag, London.
- Powell, B.S., Arango, H.G., Moore, A.M., Di Lorenzo, E., Milliff, R.F., Foley, D., 2008. 4DVAR data assimilation in the Intra-Americas Sea with the Regional Ocean Modeling System (ROMS). *Ocean Model.* 25, 173–188.
- Powell, B.S., Moore, A.M., 2009. Estimating the 4DVAR analysis error from GODAE products. *Ocean Dynam.* 59, 121–138.
- Schmitz, W.J., Biggs, D.C., Lugo-Fernandez, A., Oey, L.-Y., Sturges, W., 2005. A synopsis of the circulation in the Gulf of Mexico and on its continental margins. In: Sturges, W., Lugo-Fernandez, A. (Eds.), *Circulation in the Gulf of Mexico: Observations and Models*, vol. 161. American Geophysical Union, pp. 11–30.
- Shay, L.K., Goni, G.J., Black, P.G., 2000. The interaction between Hurricane Opal (1995) and a warm core ring in the Gulf of Mexico. *Mon. Weather Rev.* 128, 1366–1383.
- Shchepetkin, A.F., McWilliams, J.C., 2003. A method for computing horizontal pressure-gradient force in an oceanic model with nonaligned vertical coordinate. *J. Geophys. Res.* 108.
- Shchepetkin, A.F., McWilliams, J.C., 2005. The Regional Oceanic Modeling System: a split-explicit, free-surface, topography-following-coordinate ocean model. *Ocean Model.* 9, 347–404.
- Simmons, A.J., Hollingsworth, A., 2002. Some aspects of the improvement in skill of numerical weather prediction. *Q. J. R. Meteorol. Soc.* 128, 647–677.
- Talagrand, O., Courtier, P., 1987. Variational assimilation of meteorological observations with the adjoint vorticity equation. I: Theory. *Q. J. R. Meteorol. Soc.* 113, 1311–1328.
- Wang, Y.M., 2001. GSF00 mean sea surface, gravity anomaly and vertical gravity gradient from satellite altimeter data. *J. Geophys. Res.* 106, 31167–31174.
- Warner, J.C., Sherwood, C.R., Arango, H.G., Signell, R.P., 2005. Performance of four turbulence closure models implemented using a generic length scale method. *Ocean Model.* 8, 81–113.
- Weaver, A.T., Vialard, J., Anderson, D.L.T., 2003. Three- and four-dimensional variational assimilation with a general circulation model of the tropical Pacific Ocean. Part I: Formulation, internal diagnostics, and consistency checks. *Mon. Weather Rev.* 131, 1360–1378.
- Willis, J.K., Roemmich, D., Cornuelle, B., 2004. Interannual variability in upper ocean heat content, temperature, and thermocline expansion on global scales. *J. Geophys. Res.* 109, doi:10.1029/2003JC002260.
- Wilks, D.S., 1995. *Statistical Methods in Atmospheric Sciences*. Academic Press, London.